npj | quantum information

Article

Published in partnership with The University of New South Wales

https://doi.org/10.1038/s41534-024-00903-z

Optical and spin coherence of Er spin qubits in epitaxial cerium dioxide on silicon

Jiefei Zhang [1,2] ✉, Gregory D. Grant[1,3], Ignas Masiulionis[1,3], Michael T. Solomon [1,2,3], Jonathan C. Marcks [1,2,3], Jasleen K. Bindra[4], Jens Niklas [4], Alan M. Dibos [2,5,6], Oleg G. Poluektov[4], F. Joseph Heremans [1,2,3], Supratik Guha[1,2,3] ✉ & David D. Awschalom [1,2,3,7]

Robust spin-photon interfaces with optical transitions in the telecommunication band are essential for quantum networking technologies. Erbium (Er) ions are the ideal candidate with environmentally protected transitions in telecom-C band. Finding the right technologically compatible host material to enable long-lived spins remains a major hurdle. We introduce a new platform based on Er ions in cerium dioxide (CeO_2) as a nearly-zero nuclear spin environment (0.04%) epitaxially grown on silicon, offering silicon compatibility for opto-electrical devices. Our studies focus on Er^{3+} ions and show a narrow homogeneous linewidth of 440 kHz with an optical coherence time of 0.72 μs at 3.6 K. The reduced nuclear spin noise enables a slow spin-lattice relaxation with a spin relaxation time up to 2.5 ms and an electron spin coherence time of 0.66 μs (in the isolated ion limit) at 3.6 K. These findings highlight the potential of Er^{3+}:CeO_2 platform for quantum networks applications.

Rare-earth (RE) ions in dielectric solid-state hosts provide a promising platform for developing quantum memories[1–3] in quantum repeaters[1,4,5] for use in quantum communication networks. Their spin-photon interface[1,6], between matter qubits and flying photon qubits, is provided by transitions in their uniquely environmentally protected 4f shell electrons, and is characterized by long-lived spin states with a long coherence time[6] and narrow optical homogeneous linewidth[7,8]. These unique properties of RE ions have been explored to demonstrate quantum memories in atomic vapor using the DLCZ (Duan, Lukin, Cirac and Zoller) protocol[9], and in solids, using electromagnetically induced transparency[2,3], photon-echo[2,3] and atomic frequency comb[10,11]. Recently, progress on entanglement distribution[12] and quantum transduction[13,14] has also developed. All these demonstrations are enabled by a combination of RE ion and crystalline host properties.

For entanglement distribution of quantum information over long distance quantum networks, it is, hence, desirable for the matter qubits in network nodes to interface with telecommunication C-band photons to leverage existing optical fiber networks. Trivalent erbium ions (Er^{3+}) embedded in rare-earth oxides have $^4I_{13/2}$ to $^4I_{15/2}$ optical transitions in the telecom C-band and, thus, have gained attention as a candidate system aimed at developing telecom-compatible quantum memories needed in quantum repeaters. Er^{3+} long-lived optical transitions have enabled storage of information using photon-echo techniques[2,4,15] with retrieval efficiencies up to 40%[16] but with memory times limited by the optical coherence time, typically less than 1 μs. This is below the proposed requirement for quantum repeater based long-distance quantum networks[17]. To overcome the limitation on storage time, the Er^{3+} spin degree of freedom has emerged as a promising alternative to store photon information with much longer storage times[18,19], where a collective spin relaxation in the atomic ensemble is used as a local memory and reconverted to a photon through a collective interference effect[4]. Therefore, it is critical to realize long-lived spin states with coherence times orders of magnitude longer than the optical excited state lifetime for efficient optical control of the spin state and for subsequently suitable long-term quantum state storage[6,18].

As a Kramer's ion, the intrinsic non-zero electronic magnetic moment of Er^{3+} poses an intrinsic limit on the electronic spin relaxation and, therefore, the spin coherence. In addition, the presence of fluctuating magnetic field noise induced by the intrinsic electronic and nuclear spins in host materials further reduces the spin coherence[20]. Therefore, finding host materials with low natural abundance of isotopes with non-zero nuclear spins is a viable pathway towards improving spin properties for network

[1]Materials Science Division, Argonne National Laboratory, Lemont, IL, 60439, USA. [2]Center for Molecular Engineering, Argonne National Laboratory, Lemont, IL, 60439, USA. [3]Pritzker School of Molecular Engineering, University of Chicago, Chicago, IL, 60637, USA. [4]Chemical Sciences and Engineering Division, Argonne National Laboratory, Lemont, IL, 60439, USA. [5]Nanoscience and Technology Division, Argonne National Laboratory, Lemont, IL, 60439, USA. [6]Center for Nanoscale Materials, Argonne National Laboratory, Lemont, IL, 60439, USA. [7]Department of Physics, University of Chicago, Chicago, IL, 60637, USA. ✉e-mail: jfzhang@anl.gov; sguha@anl.gov

applications[6,21] without isotopic purification[6,22–24]. Promisingly, an electron spin coherence time of 23 ms has been reported for Er^{3+} at 10 mK in $CaWO_4$, which has a low nuclear spin environment with only 14% of ^{183}W isotope of natural abundant tungsten with nuclear spin of $I = \frac{1}{2}$ contributing to the spin noise in the host[25,26].

To this end, cerium dioxide (CeO_2) with cerium contributing zero nuclear spin and oxygen carrying only 0.04% (^{17}O), is a promising potential host for quantum spin $S = \frac{1}{2}$ systems with a theoretically predicted coherence time up to 47 ms[6,21]. The compatibility of CeO_2 with silicon and its engineerable piezoelectric property also make the material a good candidate for opto-electrical quantum devices. Recently, we demonstrated the molecular beam epitaxy (MBE) based synthesis of single-crystal Er-doped CeO_2 films on Si(111) substrates and the doping dependence on Er^{3+} optical and spin linewidths[27]. In this work, we make use of these films with low doping levels (3 parts-per-million (ppm)) to explore the intrinsic optical homogeneous linewidths and electron spin coherence. Using two pulse photon-echo measurements, we demonstrate that the Er^{3+} ions have long-lived optical states with a narrow homogeneous linewidth of ~440 kHz and optical coherence of ~0.72 µs at 3.6 K. Temperature dependent data suggests that the homogeneous linewidth could be <200 kHz at millikelvin temperatures with optical coherence >1 µs, indicating the promising potential of Er^{3+} in CeO_2 as a long-lived optical quantum memory. Moreover, the reduced magnetic field noise from a low nuclear spin environment in the CeO_2 film enables electron spin polarization with a slow spin-lattice relaxation, thereby enabling access to the electron spin dynamics even at 3.6 K, which is not observable in other, well studied, host materials including Y_2SiO_5, YVO_4, $CaWO_4$[26,28–30]. Here, we demonstrate Er^{3+} ions in CeO_2 with a spin coherence time $T_2 \sim 0.66$ µs at the isolated ion limit and a spin relaxation time $T_1 \sim 2.5$ ms, indicating the potential for millisecond scale spin coherence.

The combined narrow optical homogeneous linewidth and long spin relaxation time indicate the potential of such an Er-doped CeO_2 platform for efficient optical control of long-lived and coherent spin states for the development of quantum memories. It also opens the door to develop novel quantum opto-electrical devices for quantum state control and readout, leveraging the combination of a nuclear spin-free environment and a silicon-compatible platform.

Results

Er energy structure: crystal field split levels

The Er^{3+} doped CeO_2 sample is epitaxially grown on Si (111) ± 0.5° substrate using MBE (details in Methods). We grow a total thickness of 936 nm single crystal CeO_2 doped with a natural abundance of Er^{3+} isotopes with a total concentration around 3 ppm estimated based on Er beam flux. Detailed information on growth and structural characterizations can be found in prior work[27]. Er^{3+} ions have 11 electrons in the 4f shell that lead to the first two spin-orbit split multiplets as $^4I_{15/2}$ and $^4I_{13/2}$. These multiplets are further split into multiple levels due to the presence of a crystal field. Er ions substituting Ce site in the unit cell (Fig. 1 a) experience a crystal field of cubic symmetry[27,31]. Consequently, the $^4I_{15/2}$ and $^4I_{13/2}$ multiplets split into 5 levels, labeled respectively as Z_1 to Z_5 and Y_1 to Y_5, in the order from the lowest to highest energy, as shown in Fig. 1b[31]. The five levels consist of two doublets with irreducible representation Γ_6 and Γ_7 and three quartets Γ_8[31].

The $Y_1 \rightarrow Z_1$ transition allows optical control of the ground spin state with $S = \frac{1}{2}$ and is thus the focus of the study. We first probe the crystal field-split levels of the $^4I_{13/2}$ and $^4I_{15/2}$ multiplets (Fig. 1b) to identify the $Y_1 \rightarrow Z_1$ transition and the other $Y_i \rightarrow Z_j\,(i \neq 1, j \neq 1)$ levels. The crystal field split levels are probed through temperature and power dependent photoluminescence (PL) measurements. The Er^{3+} ions are excited by a 1473 nm laser, with photon energy higher than $^4I_{13/2} \rightarrow {}^4I_{15/2}$ transition. The Er^{3+} emissions are spectrally resolved using a spectrometer with a resolution of 20 GHz (0.16 nm, 84 μeV) which is sufficient to resolve crystal field split transitions that are typically in the hundreds of GHz to THz range[32]. Figure 1c shows the measured PL spectra with temperature ranging from 3.6 K to 130 K.

At 3.6 K, four emission peaks are observed and identified as Y_1 to $Z_1 - Z_4$ transitions (black arrows in Fig. 1(c)) due to the rapid non-radiative relaxation of electrons from higher Y levels to Y_1 level. The lack of emission from the Z_5 level may be due to its small transition dipole moment. The higher Y levels are probed by altering the Boltzmann distribution of electrons through increasing the sample temperature. These levels are thus identified based on their temperature-dependent behavior and their energy separation between each other. We observe clearly the Y_1 to Y_4 levels (non-black arrows in Fig. 1c, and more details see Supplementary Informaition (SI) Sec. 2). The Y_5 level transitions may be shorter than 1500 nm and thus not collected in the measurement setup (see SI Sec. 1). The intensity of emission from these identified Y_1 to Y_4 levels also matches the expected behavior from a Boltzmann distribution of electrons at these temperatures (see SI Sec. 2 and Fig. S2). The table shown in Fig. 1d summarizes the energy structure of the Z_1 to Z_5 and Y_1 to Y_5 levels.

The $Y_1 \rightarrow Z_1$ transition is found to be at 1530.74 nm (195.84 THz). It is separated from the Y_2 level by 1.13 meV (281.9 GHz) and from the Z_2 level by 1.51 meV (357.5 GHz). As shown later, this transition also has a narrow optical homogeneous linewidth. All studies on optical homogeneous linewidth, electron spin coherence, and electron spin relaxation are carried out at 3.6 K. Given the energy separation between the the Z_1 and Z_2, there is around 0.8% electron population of the Z_2 level. Thus, in all optical measurements resonantly addressing the $Y_1 - Z_1$ transition, one can treat the system as an effective two-level system involving only Z_1 level and ignore the population of electrons at higher Z levels. However, for spin measurements, the population of the Z_2 level becomes significant in the study of spin relaxation dynamics of Z_1 level, as will be discussed later.

Optical coherence

With the identification of the crystal field split levels of the $^4I_{13/2} \rightarrow {}^4I_{15/2}$ transition, we focus on the $Y_1 \rightarrow Z_1$ transition to probe the inhomogeneous and homogeneous linewidths. All measurements are done at 3.6 K without external magnetic field. The inhomogeneous linewidth is probed using photoluminescence excitation spectroscopy (PLE, pulse sequence in the inset of Fig. 2a, details in Methods). Figure 2a shows the measured spectrum while scanning the laser frequency across the $Y_1 - Z_1$ transition with a step size of 0.625 GHz. The Lorentzian fit to the data indicates an inhomogeneous linewidth of $\Gamma_{inh} = 9.5 \pm 0.2$ GHz (0.07 nm or 39 μeV), comparable to other MBE grown Er^{3+} doped in other rare-earth oxide films such as Y_2O_3 and TiO_2[33,34]. Compared with Er^{3+} ions in other bulk low nuclear spin host materials, such as YSO (Y_2SiO_5), Y_2O_3, and $CaWO_4$, the observed linewidth is around a factor of ten higher[35–37]. This is likely due to the relative high density of threading dislocations and unintended defects in the epitaxial CeO_2 film on Si originating from the 0.5% lattice mismatch induced strain[27]. The observed signal is dominantly from nuclear spin zero Er ions (^{166}Er, ^{168}Er and ^{170}Er), ^{166}Er being the dominate isotope. The emission from the 23% of ^{167}Er is buried under the observed broad inhomogeneous peak.

Besides inhomogeneous linewidth, the homogeneous linewidth is another important figure-of-merit for an optical transition. One can extract the homogeneous linewidth through the measurement of optical coherence (T_2) where $\Gamma_{hom} = \frac{1}{\pi T_2}$[38], and we do so via two-pulse photon-echo (PE) measurement. Figure 2b shows the measured integrated echo intensity as a function of time delay, τ, between the two pulses at 3.6 K using the pulse sequence schematically shown in the inset (details in Methods and SI Sec. 3). The data show a single exponential decay envelope of the photon echo amplitude modulated with an oscillating beat pattern. The beat pattern indicates that we are coherently addressing a superposition of two transitions in a three-level system with the energy separation of two of the levels being within the bandwidth of the optical pulse. The red line is a fit to the data considering a single exponential decay with an added frequency of oscillation $f = 1/T_{osc}$. The data indicate an optical coherence $T_2 = 720.0 \pm 33.1$ ns with homogeneous linewidth $\Gamma_{hom} = \frac{1}{\pi T_2} = 442.1 \pm 20.3$ kHz and a beat period of $T_{osc} = 300.2 \pm 11.8$ ns ($f_{osc} = 3.33 \pm 0.23$ MHz). The observed beat frequency is within the bandwidth of the optical pulse and also found to be consistent with the Zeeman splitting of the Z_1 level due to earth's magnetic field at around 0.35 G. This suggests that the beat might be from the earth's magnetic field lifting the degeneracy of Z_1 level.

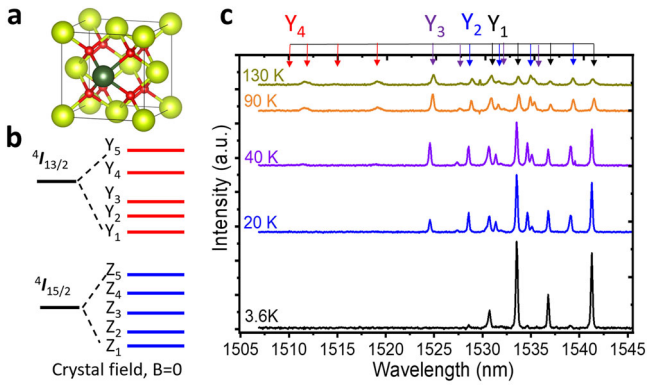

Fig. 1 | Crystal field split energy levels of the $^4I_{15/2}$ and $^4I_{13/2}$ multiplets of Er^{3+} ions in CeO_2. a Schematic of a CeO_2 unit cell with an Er ion (dark green) substitutionally incorporated into a Cerium (light green) site. **b** Schematic of the crystal field splitting of the $^4I_{15/2}$ and $^4I_{13/2}$ multiplets, with 5 levels each, labeled as Z_1 to Z_5 and Y_1 to Y_5. **c** Temperature dependent PL spectra of Er^{3+} ion emission with Er^{3+} ion excited by a 1473 nm laser with excitation power of 1000 μW on the sample surface, 5 times the power needed to saturate $Y_1 - Z_1$ level transition (details in SI Sec. 2). **d** Table summarizing the crystal field split energy levels.

The observed homogeneous linewidth, Γ_{hom} = 442.1 ± 20.3 kHz, at 3.6 K is orders of magnitude higher compared to the lifetime-limited Γ_{hom} ~94 Hz given the ~ 3.4 ms radiative lifetime[27] of the $Y_1 - Z_1$ transition. However, the observed Γ_{hom} is similar to that reported in bulk YSO which shows ~ 80 kHz at 1.6 K[39] and ~ 300 kHz around 4 K[40]. Insight into dephasing mechanisms in the material is obtained from the temperature dependent evolution of Γ_{hom} from 3.6 K to 5.5 K. The Γ_{hom} for rare-earth ions typically results from several contributions including (i) excitation-induced interaction between active ions, proportional to the concentration of excited ions, and leading to the phenomenon of instantaneous spectral diffusion (ISD)[41]; (ii) the interaction between active ions and surrounding electron and nuclear spins from host lattice ions, other dopant ions, and magnetic defects, inducing active ion spin-flip[40]; (iii) interactions with lattice phonons[42,43]; (iv) perturbations due to tunneling between nearly equivalent configurations, also known as two-level systems (TLS) and presenting linear dependence on temperature[44–46]; and (v) electric interaction with free electrons, charged defects and dangling bonds[47]. At this examined temperature range, we are probing the interaction with TLS and phonons with dominant phonon process being Orbach process while all the rest temperature independent processes are captured in a constant Γ_0 as shown in Eq. (1). Figure 2c shows the extracted Γ_{hom} as a function of temperature, T. The beat frequency extracted from all temperatures (Fig. 2d) is independent of temperature, consistent with its origin in the Zeeman splitting of the Z_1 level induced by the earth's magnetic field. The observed $\Gamma_{hom}(T)$ dependence indicates that the increase in $\Gamma_{hom}(T)$ is dominated by Orbach relaxation[42,43]. The solid line is the fit to the data using Eq. (1):

$$\Gamma_{hom}(T) = \Gamma_0 + \alpha_{TLS} \cdot T + \alpha_{phonon} \cdot exp\left(\frac{-\Delta E}{k_B T}\right) \quad (1)$$

where α_{TLS} is the coefficient for coupling to TLS, α_{phonon} is the coefficient for coupling to Orbach phonon process, and k_B is the Boltzmann constant.

The fitting indicates a Γ_0 of 286 ± 77 kHz, α_{TLS} = 3.2 ± 1.8 kHz/K, α_{phonon} = 91.9 ± 16.6 MHz with a ΔE of 2.08 ± 0.36 meV, consistent with the energy separation between the Z_1 to Z_2 level obtained from PL measurements. Of the total linewidth broadening, around 150 kHz is due to coupling to an Orbach process at 3.6 K with the remaining 300 kHz of broadening coming from the combined contribution of Γ_0 and coupling to TLS. The obtained coupling to TLS is consistent with the typical reported value of a few to tens of kHz/K[42,48,49] for rare-earth ions in oxides. One can thus deduce that Γ_0 is most likely ≤ 200 kHz at sub-Kelvin temperatures (optical coherence >1 μs). This suggests that the dominant dephasing process contributing to Γ_0 might be from spectral diffusion due to ion-ion dipolar interactions, optical excitation induced ISD and ground- and excited-state spin-flip rates from interaction with Er ions as well as other dopant ions and magnetic defects[40]. Additionally, fluctuating field induced by background charge and defects as well as strain in the film from CeO_2/Si interface could also induce added spectral diffusion which is a negligible contribution for bulk crystals like YSO. It is worth noting that the sample studied here is grown without any optimization for the optical linewidth. One can further improve on the homogeneous linewidth by optimizing growth to reduce strain induced defects including vacancies and dislocations causing fluctuating electric field and minimize unintentional defects. There is also the path of reducing the concentration of Er^{3+} to minimize ISD. Besides this, one can also improve the homogeneous linewidth by applying moderate magnetic field to reduce the coupling of TLS to the dipole moment of Er^{3+} and the Er spin flip-flop process[35,40,42].

The obtained homogeneous linewidth suggests that a viable path exists for further engineering the light-matter interaction via integrating Er ions in a cavity with a suitable quality factor to enhance the radiative transition rate, through the Purcell effect, close to its optical coherence limit[50,51], all in an integrated silicon-compatible opto-electrical device. Further improvement on the homogeneous linewidth through growth optimization and reduction of spectral diffusion and phonon-mediated dephasing at millikelvin temperature with external magnetic field can aid in reaching sub-kHz homogeneous linewidths and radiative-lifetime limited coherent photon generation, necessary for coherent optical control of the Er spin states.

Electron spin coherence

The optical coherence study discussed earlier indicates that Er^{3+} ions in CeO_2 show a narrow optical homogeneous linewidth with promising potential of providing up to several microseconds of optical coherence at millikelvin temperatures. For the application and use of Er^{3+} as the spin-photon interface for quantum memory, the Er^{3+} electron spin coherence is the other important figure-of-merit. We use a X-band (9.7 GHz) pulsed electron paramagnetic resonance (EPR) spectrometer to study Er^{3+} electron spin coherence and relaxation. Figure 3a shows the measured spin echo response as a function of the static magnetic field. The data are taken with a fixed time delay, τ, of 100 ns between the $\pi/2$ and π pulses. The resultant spectrum shows the expected resonance from nuclear-spin-zero even isotopes (dominantly $^{166}Er^{3+}$, primary peak) along with the hyperfine levels of 23% of the $^{167}Er^{3+}$ with nuclear spin $I = \frac{7}{2}$ (smaller secondary peaks), consistent with results in prior work[27]. Seven of the eight hyperfine peaks are spectrally resolved with one of the hyperfine resonances hiding under the primary resonance peak at B_0 = 0.102 T. The solid line is fit to the data including the Zeeman and hyperfine terms while also accounting for the second-order perturbation effects from the large nuclear spin of $^{167}Er^{3+}$. The extracted g value is g = 6.828 ± 0.005, consistent with the CW EPR work[27]. The g value matches theoretical estimates and reported values for Er^{3+} in CeO_2 nanocrystals[31,52]. The obtained linewidth of the Er^{3+} spin resonance is

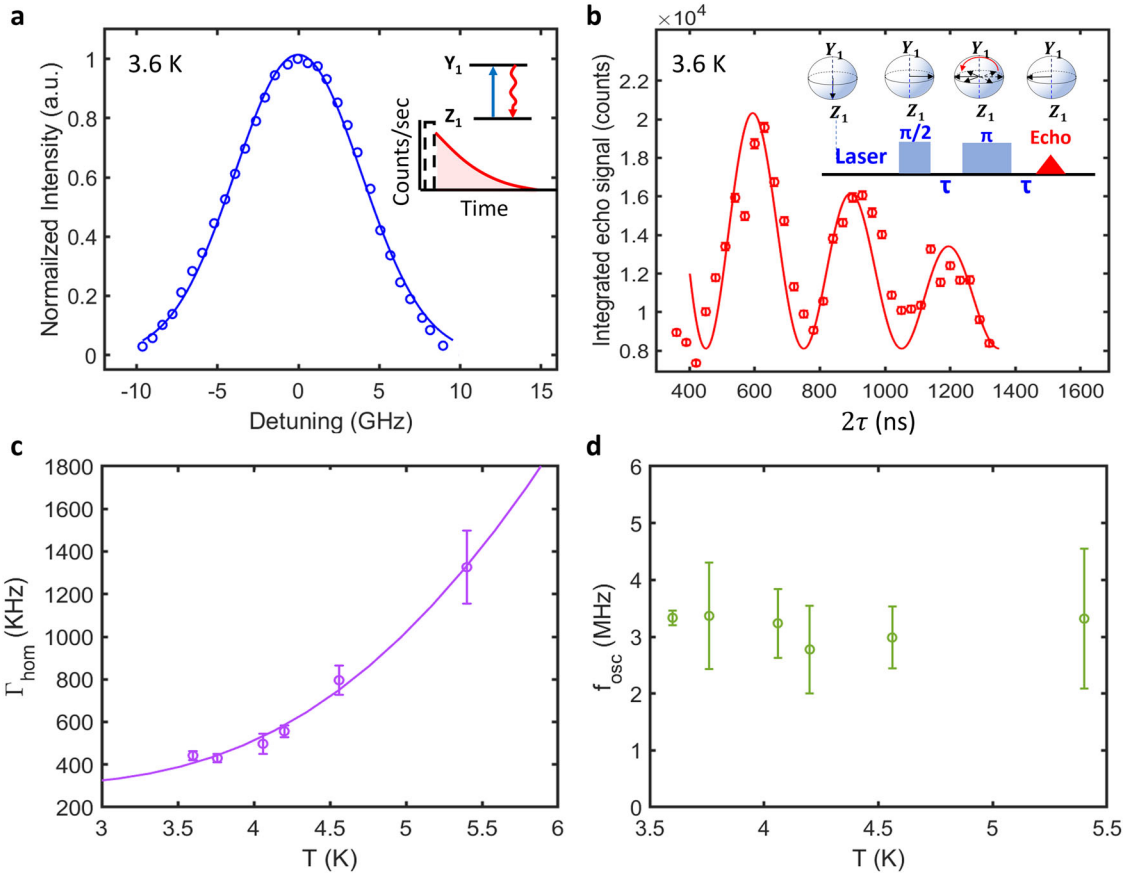

Fig. 2 | Optical homogeneous linewidth and optical coherence of $Y_1 - Z_1$ transition. a PLE fine scan of $Y_1 - Z_1$ transition with a step size of 0.625 GHz (2.6 μeV) at 3.6 K with data shown as open circles. The Lorentzian fit to the data is shown as the solid curve, indicating an inhomogeneous linewidth of Γ_{inh} = 9.5 ± 0.2 GHz. The inset shows the schematic of the employed pulse sequence. **b** Two-pulse photon echo (PE) decay for the $Y_1 - Z_1$ transition with the pulse sequence shown in the inset and data shown as open circles. The solid line is the fit to the data, indicating optical coherence T_2 = 720.0 ± 33.1 ns and homogeneous linewidth Γ_{hom} = 442.1 ± 20.3 kHz. The observed beating pattern is of beating period T_{osc} = 300.2 ± 11.8 ns (f_{osc} = 3.33 ± 0.23 MHz). **c** Temperature dependence of Γ_{hom} measured by two-pulse PE with data shown as open circles. The solid line is the fit to the data using Eq. (1). **d** Plot of the extracted f_{osc} (open circles) from two-pulse PE measurement as a function of temperature.

2.57 ± 0.03 mT (244.9 ± 2.9 MHz), consistent with CW results[27]. This confirms the expected EPR resonance of Er^{3+} ion in a crystal with cubic crystal field symmetry and a Z_1 level of representation Γ_6. The observed linewidth is probably limited by the Er dipole-dipole interaction and interaction with Er dopant-driven defects (i.e. oxygen vacancies and defect complexes) in the film[27].

The Er^{3+} spin coherence time, T_2, is probed via Hahn-echo measurement. The magnetic field is tuned to the resonance of the primary peak at B = 0.102 T (Fig. 3a) under the applied 9.7 GHz microwave frequency. The echo signal is predominantly from the ^{166}Er electrons with only 3.6% of the signal from the ^{167}Er electrons. Figure 3b shows the measured spin echo signal collected as a function of the delay (τ) between the $\pi/2$- and the π-pulse at 3.6 K. From the fit of $I \propto \exp(-2\tau/T_2)$ (black curve in Fig. 3b), one obtains T_2 = 0.249 ± 0.035 µs. The low nuclear spin noise enables access to the electron spin coherence dynamics at such elevated temperature, which is not observable in other well studied host materials including YSO, YVO_4, $CaWO_4$[26,28–30]. Similar to optical Γ_{hom}, the spin T_2 is typically controlled by the phonon induced dephasing at such elevated temperatures, magnetic TLS[49], interaction of Er ions with possible magnetic defects in the host[40], and spin excitation induced ISD between Er ions[53–55]. To understand the dominant dephasing mechanics, we carry out instantaneous diffusion measurements[53,55] to probe and decouple the Er-Er spin dipolar interactions using a generalized Hahn echo sequence ($\pi/2 - \tau - \theta$). We vary the angle, and hence the fidelity, of the second inversion pulse[53,54]. The second pulse inhibits the decoupling of the probed spins' mutual dipolar interactions, resulting in slower decoherence through instantaneous diffusion. The spin echo signal (SE) is thus proportional to the exponential of the averaged inversion pulse fidelity $\langle \sin^2(\theta/2) \rangle$ and is given by[53]:

$$SE(\tau) \propto exp\left(\frac{8\pi^2}{9\sqrt{(3)}}\frac{g^2\beta^2}{\hbar} N \sin^2(\theta/2)\tau\right) \quad (2)$$

where N is the total number of spins per m^3 and β is the Bohr magnon. Thus, the spin decoherence from instantaneous diffusion, $T_{2,INST}$, is proportional $\langle \sin^2(\theta/2) \rangle$. One has the following equation for T_2 with $T_{2,INST}$ representing the contribution from ISD and $T_{2,bath}$ representing the combined effect of phonon, magnetic TLS and interaction of Er with possible magnetic defects (details see SI. Sec. 6):

$$\begin{aligned} 1/T_2 &= 1/T_{2,INST} + 1/T_{2,bath} \\ &= \frac{8\pi^2}{9\sqrt{(3)}}\frac{g^2\beta^2}{\hbar} N \sin^2(\theta/2) + 1/T_{2,bath} \end{aligned} \quad (3)$$

In the instantaneous diffusion measurements, the angle of the second rotation pulse θ is varied by tuning the power of the microwave pulse (see SI Sec. 5), while keeping the pulse length, and thus bandwidth, unchanged. Figure 3c shows the measured echo intensity as a function of τ with three different rotation angles θ. A reduction of rotation angle θ reduces the effective population of spins flipped by the microwave pulse, thus improving the decoupling of these spins from the instantaneous diffusion decoherence. Er spin T_2 under this measurement increases from 0.25 µs to 0.58 µs. The

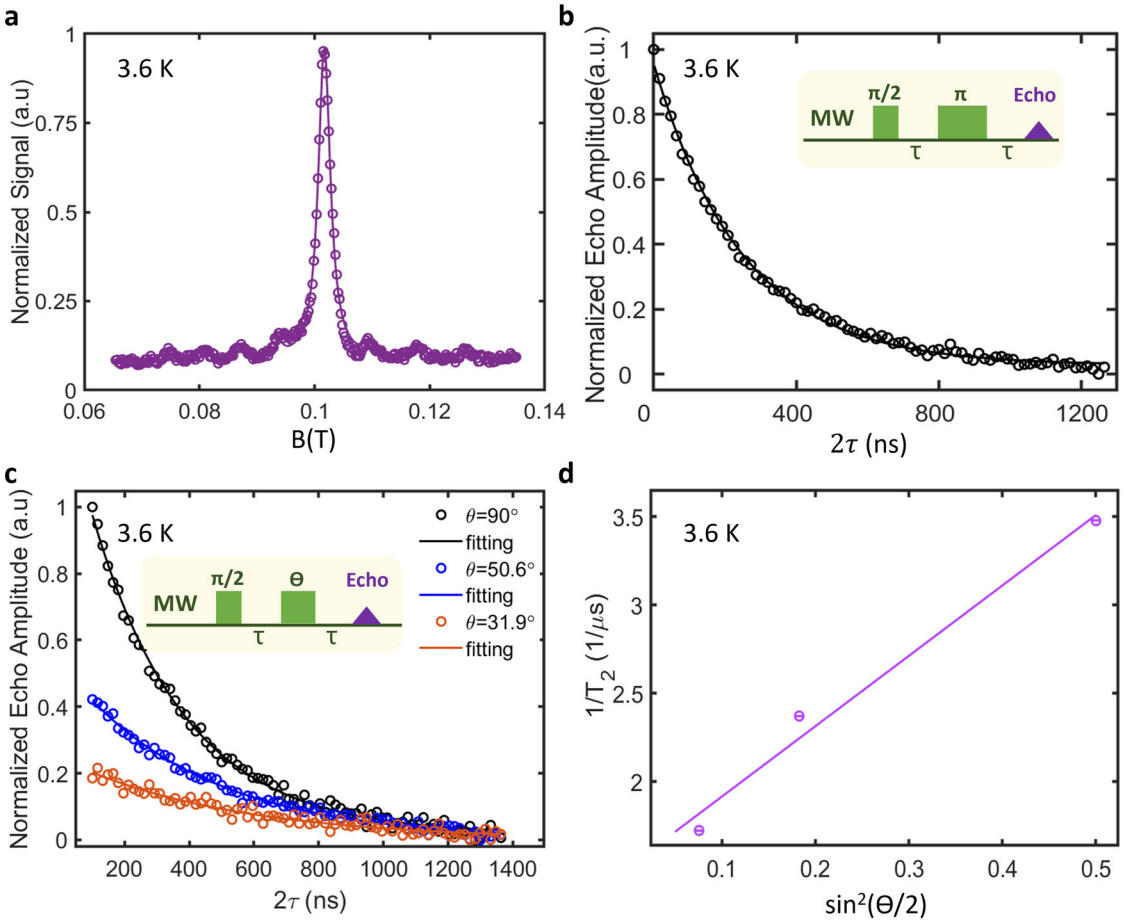

Fig. 3 | Electron spin coherence at 3.6 K probed by pulsed EPR with microwave drive at 9.7 GHz. a Resultant EPR spectrum from two-pulse echo as the magnetic field (B) is swept. Data is taken using the Hahn-echo sequence schematically shown in **b** with fixed delay time (τ = 100 ns) between the $\pi/2$ pulse and π pulse. **b** Spin echo measurement using two-pulse Hahn-echo sequence, schematically shown in the inset. Data (open circles) are taken as a function of time delay τ between the $\pi/2$ pulse and π pulse. The solid black line is a single exponential fit revealing the spin coherence time T_2 = 0.249 ± 0.035 μs. **c** Generalized Hahn echo measurements on Er^{3+} electron spins taken with three different flip angles θ of the second rotation pulse. Solid lines are the single exponential fits to the data. **d** Plot of the inverse of spin coherence time T_2, extracted from the fits to the data in **c** as a function of averaged inversion pulse fidelity $\langle\sin^2(\theta/2)\rangle$. Linear fit to the data (solid line) yields the spin coherence at single isolated ion limits to be T_2 = 0.660 ± 0.04 μs and a spin concentration of 5.66 ± 0.25 ppm in the sample.

inverse of the extracted T_2 obtained through the single exponential fit to data in Fig. 3c is shown in Fig. 3d. Following Eq. (3), the slope of the linear fit to the data in Fig. 3d yields the density of probed Er spins to be $1.66 \pm 0.08 * 10^{22}/m^3$, 0.68 ± 0.03 ppm. Accounting for the fraction of probed Er out of the entire ensemble (12% probed), the estimated total concentration of the Er spin is 5.66 ± 0.25 ppm, within a factor of 2 of the Er concentration estimated from Er flux used during MBE growth. The intercept of the linear fit provides an estimate on the spin coherence at the single isolated ion limit, where ion-ion dipolar interactions within the ensemble do not limit decoherence, of $T_2 = T_{2,\text{bath}} = 0.660 \pm 0.004$ μs. Thus, the measured T_2 in Fig. 3b is largely limited by the Er-Er spin dipolar interaction-induced instantaneous diffusion and could be improved by reducing Er concentration. With the generalized echo sequence reducing instantaneous diffusion, the spin homogeneity $\Gamma_h = \frac{1}{\pi T_2}$ contributed by the bath is 484.8 ± 20.6 kHz. The deduced spin coherence $T_{2,\text{bath}}$ at the single isolated ion limit is probably dominated by the spectral diffusion induced by interaction with other defects in the film and coupling to magnetic TLS (see SI. Sec. 6).

Electron spin relaxation

The upper limit on spin coherence is set by the spin relaxation. The spin relaxation time is probed by first applying a π-pulse to invert the population of spin-up and spin-down electron states, and then reading out the relaxation of spin-up to spin-down states using the two-pulse Haho-echo sequence (schematically shown in Fig. 4a, details see Methods). By varying the delay time, τ, between the inversion pulse and the $\pi/2$-pulse, one can map out the spin relaxation dynamics. Figure 4a shows the measured spin echo amplitude as a function of τ measured at 3.6 K. The data indicates the presence of two spin relaxation channels with a short spin relaxation T_1 = 0.11 ± 0.01 ms and a long relaxation T_1 = 0.83 ± 0.04 ms. The two observed decay processes might come from the electron depopulation of the Z_1 spin level to its nearby Z_2 level, resulting in a sampling of electron population between three active states[56]. EPR is an inductive detection method that is sensitive to the population of ground states. The possible depopulation of Z_1 spin-up level to Z_2 spin level, mediated by phonon processes, can thus be detected by pulsed EPR.

To further probe the origin of the observed double exponential decay dynamics, we carry out optical measurements of spin relaxation T_1 of the Z_1 level at 3.6 K. We apply a 100 mT magnetic field parallel to the $\langle 1\bar{1}0\rangle$ direction, with orientation chosen to be the same as that used in the pulsed EPR measurements. A Zeeman splitting of 9.46 GHz between the spin-up and spin-down state of the Z_1 level is induced, estimated based on the effective g value extracted from data shown in Fig. 3a. Given that the spin T_1 is shorter compared to the optical lifetime of the $Y_1 - Z_1$ transition, the optical measurement of spin T_1 cannot be done using typical spectral hole-burning method[57,58], where one can fully polarizes the spins through the

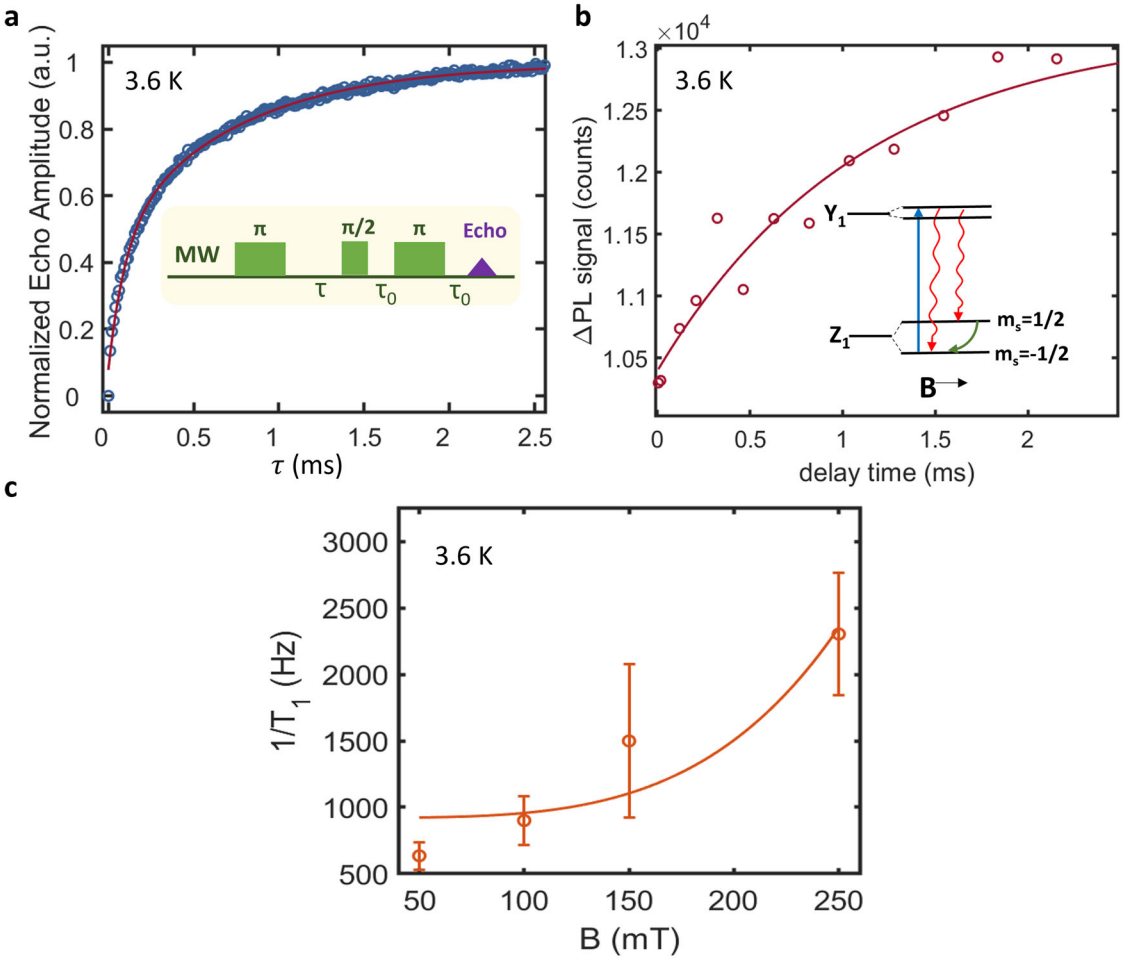

Fig. 4 | Electron spin relaxation dynamics at 3.6 K. a Pulsed EPR based spin echo measurement with a three-pulse population inversion sequence (see Methods) shown in the inset. The measured data are shown as open circles (error within circles size) and the solid line is a double exponential fit revealing two spin relaxation paths with a short spin relaxation $T_1 = 0.11 \pm 0.01$ ms and a long relaxation $T_1 = 0.83 \pm 0.04$ ms. **b** Optical measurement of Z_1 level spin relaxation using two optical pulses using pump and probe scheme. The panel shows the measured PL signal difference (ΔPL, open circles, errors within circle size) with and without the second probe optical pulse as a function of time delay τ between pulses. Data are taken with laser resonant to the spin-down Z_1 to spin-up Y_1 level transition (inset). A 100 μs pulse is applied first followed with a second 100 μs pulse separated by τ. PL signal is collected within a 4 ms collection window with 15,000 iterations of measurements. Details on the pulse sequence is in SI Sec. 7. **c** Optically measured spin relaxation time T_1 as a function of the applied magnetic field. The plotted T_1 is the fitted value extracted with 95% confidence from each measured ΔPL data show in Fig. S8 in SI Sec. 7. The data show an increase of 0.437 ms to 1.575 ms by reducing the field strength from 250 mT to 50 mT.

cumulative optical excitation processes. Here we use a two-pulse based pump-probe scheme to probe the spin relaxation from spin up to spin down state through examining population inversion recovery of the spin down states. We first apply a short 100 μs optical pulse resonant to the transition between Z_1 spin down state and the Y_1 spin up state (inset of Fig. 4b) to create an initial state occupation where the population of the Z_1 spin-up state is higher than that of spin-down states. A second pulse of 100 μs is applied after a delay, τ, to probe the recovery of the spin-down state occupation due to spin relaxation. A reference measurement without the second excitation pulse is taken to sample the photon emission into collection window from optical decay of the Y_1 level to both spin states after the first optical pulse as the background for subtraction (details in SI Sec. 7).

Figure 4b shows the measured difference of the PL signal, ΔPL, collected during the collection window with and without the second optical pulse as a function of τ between the two optical pulses. The spin recovery from spin-up to spin-down through spin relaxation is evidenced by the increasing ΔPL with τ. The data shows a single exponential decay (fitting, solid line) indicating a spin relaxation time for the Zeeman split Z_1 spin-up to spin-down state of $T_1 = 1.106 \pm 0.256$ ms. The measured T_1 value is consistent with the long T_1 resolved in the pulsed EPR shown in Fig. 4a. It also suggests that the short T_1 of 0.11 ms observed in pulsed EPR measurement is most likely coming from the phonon mediated depopulation of electrons from Z_1 spin up level to Z_2 level.

The observed spin T_1 is longer compared to that of Er in YSO[59] probably due to reduced phonon coupling processes. At this temperature, the spin relaxation time T_1 of the ground state is limited by phonon-mediated processes, including direct, Raman and Orbach processes[60] and spin flip-flop induced by interaction with other ions and magnetic defects[61]. One can further extend the relaxation time by tuning the magnetic field to control the direct coupling process, which can be suppressed with lower magnetic field by reducing the number of phonon modes that can couple to the Zeeman split states as[49,61]:

$$T_1^{-1} = R_o + A_f(g^4)\mathrm{sech}^2\left(\frac{g\mu_B B}{2k_B T}\right) + A_d\left(\frac{g\mu_B B}{h}\right)^5 \coth\left(\frac{g\mu_B B}{2k_B T}\right) \quad (4)$$

The last term corresponds to the direct phonon process and is proportional to B^4T when the Zeeman split Z_1 level $g\mu_B B$ is less than $2k_BT$ [62], where the

parameter A_d characterizes the strength of the phonon coupling with h the Planck's constant. The second term represents the average rate of mutual spin flip-flops[49], i.e., exchange of spin states between two Er ions, which is affected by the magnetic field with A_f the coupling constant, g the g factor of the ions, μ_B the Bohr magneton and k_B the Boltzmann constant. The constant R_o represents all residual relaxation processes including Orbach and Raman processes at fixed temperature studied here. Figure 4c shows the measured spin T_1 time as a function of the magnitude of the applied magnetic field. We measure T_1 with B-field at 50 mT, 100 mT, 150 mT and 250 mT. The T_1 values are extracted from measured ΔPL data shown in Fig. S8 in SI Sec. 7 using the same two optical pulse sequence. We observe an extension of T_1 from $T_1 = 1.106 \pm 0.256$ ms to $T_1 = 1.575 \pm 0.256$ ms when reducing the field strength from 100 mT to 50 mT, and similarly a reduction of T_1 to 0.4345 ± 0.087 ms at an elevated field of 250 mT. The solid line shown is a fit to the T_1 data using Eq. (4). The fitted coefficients are $R_o = 401.2 \pm 80$ Hz, $A_f = 0.24 \pm 0.07$ Hz and $A_d = (2.99 \pm 0.08) \times 10^{-5}\ s^{-1}GHz^{-5}$. The fitting suggests that one can further extend the spin T_1 to 2.5 ms at 3.6 K. The A_d is smaller compared to that for Er in YSO[59] which indicates a weaker phonon coupling, consistent with the observed ms long spin T_1. The A_f is also smaller compared to reported values for Er in YSO and V_2O_3[40,57,63]. The smaller coupling parameters are consistent with the cubic crystal symmetry in CeO_2[62]. The observed spin T_2 in the single-ion limit is 0.66 μs, much less than the observed spin T_1. The long T_1 and the low coupling to TLS revealed from optical coherence study indicates that spectral diffusion induced by Er coupling to other defects (i.e oxygen vacancies and defect complexes, details in SI. Sec. 6) is the other limiting process for spin coherence besides the spin excitation induced ISD. With growth optimization and post-growth treatments to reduce unintended defects and freezing this dipolar interaction induced spin flip at moderate fields with millikelvin temperatures, one could reach the T_1 limited spin T_2 at millisecond time scale.

Discussion

Our work on Er-doped CeO_2 hightlights the potential of this material system as a robust optical quantum memory platform owing to its narrow linewidth and long-lived optically addressable electron spin, enabled by the low nuclear spin host environment. The observed homogeneous linewidth of 440 kHz for the $Y_1 - Z_1$ transition and electron spin relaxation time of 2.5 ms at 3.6 K indicate the feasibility of using collective electron spin relaxation as a local quantum memory for quantum repeaters. The narrow homogeneous linewidth also demonstrates the potential for integrating Er^{3+} with nanophotonic cavities to achieve Purcell enhancement and near Fourier transformation-limited single-photon emission. This would allow for coherently driven optical transitions at a desired rate to address individual ions[50,64] and examine the time-dependent spectral diffusion of individual Er^{3+} ions in the host[8], a critical step towards entanglement distribution needed for quantum repeaters. The significant reduction in the concentration of nuclear magnetic moments in CeO_2 compared to that of other hosts, such as Y_2SiO_5 and YAG, could open a path towards not only long-lived coherent Er^{3+} electron spin states, but also long-lived nuclear spins in isotopically enriched ^{167}Er to enable long storage times on the scale of seconds, using both collective relaxation modes of nuclear spin ensembles[18] and individual nuclear spin states[65,66].

The Er^{3+} spin ensemble coherence time reported here is largely limited by the ion-ion dipolar interaction. As indicated by the instantaneous diffusion measurements, in the single-ion limit, the Er^{3+} spin coherence T_2 is around 0.66 μs. One can be further improve spin coherence by lowering the temperature below the explored 3.6 K in this work to millikelvin temperature and also by using higher magnetic fields to freeze spin-flip induced dephasing. The MBE growth of Er-doped oxides also enables the control of Er doping levels and optimization of material quality. Continued growth optimization employing slower growth rate with a lower oxygen pressure[67] to suppress dislocation and unintended defect formation may enable high quality single crystal CeO_2, thereby reducing spectral diffusion and improving both optical and spin properties. It can also enable growth of CeO_2 thin films with controlled delta doping of Er to create structures compatible with integration with nanophotonic cavities, either within the oxide or hybrid structures integrated with other dielectric materials. The sample studied here is grown without growth optimization yet already demonstrates appreciable spin relaxation (~2.5 ms) and narrow optical homogeneous linewidths (440 kHz). Thus, Er^{3+} in CeO_2, an oxide host with a very low nuclear spin environment, could emerge as a versatile platform for highly coherent silicon compatible light-matter quantum interfaces for quantum communication applications.

There are also challenges ahead. One that remains is device fabrication in CeO_2. CeO_2 is a hard material but is amenable to carbon tetrafluoride and chlorine-based dry etch chemistry[68,69] as well as acidic based wet etch chemistry[69] for top-down photonic device fabrication. The difficulty lies in realizing the needed anisotropic etching with high selectivity with respect to Si and SiO_2. As such, further development of the etching process is needed. Additionally, one would also need to tackle the CeO_2 thin film growth on Si (100) for integration with Si (100) SOI (Silicon-On-Insulator) or develop Si (111) SOI to interface CeO_2 (111) film. Besides this fabrication challenge, there are also the added possible challenges from extending both optical and spin coherence time. The cubic symmetry and smaller crystal field of Er in CeO_2 indicate weaker spin-phonon coupling showing great potential for long-lived spin state. However, the isotropic g factor, coming from the cubic symmetry, leads to a stronger Er-Er interaction and Er-defects interaction in CeO_2 compared to other hosts. Thus, it could imply strict experiment conditions for operating such platforms including low Er concentration (ppb level, parts per billion), millikelvin temperature as well as high magnetic field to freeze dipolar interaction induced spin flip-flop. Furthermore, one also needs better control on material quality to minimize unintended defects and dopants to reduce interaction between these and targeted Er ions. Careful examination of these are needed to enable simultaneous achievement of long optical and spin coherence which is key for quantum memory applications.

Methods

Sample and growth

The Er-doped CeO_2 film studied here is grown on silicon (111) ± 0. 5° using MBE. Single crystal CeO_2 is grown at a sample temperature of 670°C with a growth rate of 312.1 nm/hr under oxygen pressure of 4.9e-6 torr and Ce/O_2 flux ratio ~20. The grown CeO_2 layer is 936.3 nm thick with Er-doped through the entire grown layer with an estimated Er concentration of 3 ppm, based on the erbium flux delivered during growth[27]. Details on growth condition and structural characterization of as-grown films can be found in ref. 27. The as-grown sample is directly used for all the measurements shown here without any post-growth processing.

Optical pulse sequences for optical measurements

All optical data shown in the main text are collected at 3.6 K with Er emission collected using time gating method. For PLE measurements (Fig. 2(a)), 1.5 ms long optical pulse with wavelength tuned across $Y_1 - Z_1$ transition is used to excite the Er ions. A collection window of 7 ms after the excitation pulse is used to collect the emission from Er ions. The collection window is chosen based on the optical lifetime of the $Y_1 - Z_1$ transition (3.4 ms, ref. 27) to enable needed signal-to-noise. For photon echo measurements (Fig. 2b and c), 10 ns $\pi/2$-pulse followed with a 20 ns π-pulse after a delay τ is used. The laser is set to be resonant with the $Y_1 - Z_1$ transition with laser power tuned to reach needed $\pi/2$ and π pulse area (see SI Sec. 3). The shortest possible pulse enabled by our instrumentation is used to minimize dephasing during the excitation process. Data are collected with τ ranging from 180 ns to 700 ns. Details on instrumentation for all optical measurements are captured in SI Sec. 1 and 7.

Pulsed EPR measurements

X-Band (9.7 GHz) EPR experiments are taken using an ELEXSYS E580 spectrometer (Bruker Biospin, Ettlingen, Germany) that is equipped with a dielectric ring resonator (Bruker ER 4118X-MD5) as shown in Fig. S4 in SI Sec. 4. The Er-doped CeO_2 film on Si samples are diced to a size of 4 mm

x 2.5 cm and mounted into a quartz tube suspended in the center of the dielectric ring resonator contained in a flow cryostat (Oxford Instruments CF935) with pumped liquid helium. The data shown in the manuscript are obtained at 3.6 K with temperature controlled by an ITX temperature controller (Oxford Instruments). For spin echo field sweep (Fig. 3a), two-pulse Hahn echo sequence is applied with a 12 ns π/2-pulse followed by a 24 ns π-pulse with a fixed delay τ of 100 ns. The pulse length is chosen for the shorted achievable length to cover large size of Er spin ensemble. For spin coherence measurement (Fig. 3b), the same Hahn echo sequence is used with a varying delay τ ranging from 100 ns to 1300 ns. For spin relaxation measurement (Fig. 4a), three-pulse population inversion sequence is used where a 24 ns π-pulse is followed by a two-pulse Hahn echo sequence with varying time delay τ. The two-pulse Hahn echo sequence used here is composed of a 12 ns π/2-pulse followed by a 24 ns π-pulse with a fixed delay τ of 100 ns.

Data availability

The data that support the findings of this study are available from the corresponding author upon reasonable request.

Received: 12 December 2023; Accepted: 10 October 2024;
Published online: 20 November 2024

References

1. Awschalom, D. D., Hanson, R., Wrachtrup, J. & Zhou, B. B. Quantum technologies with optically interfaced solid-state spins. *Nat. Photonics* **12**, 516–527 (2018).
2. Lvovsky, A. I., Sanders, B. C. & Tittel, W. Optical quantum memory. *Nat. Photonics* **3**, 706–714 (2009).
3. Heshami, K. et al. Quantum memories: emerging applications and recent advances. *J. Mod. Opt.* **63**, 2005–2028 (2016).
4. Sangouard, N., Simon, C., de Riedmatten, H. & Gisin, N. Quantum repeaters based on atomic ensembles and linear optics. *Rev. Mod. Phys.* **83**, 33–80 (2011).
5. Awschalom, D. et al. Development of quantum interconnects (quics) for next-generation information technologies. *PRX Quantum* **2**, 017002 (2021).
6. Wolfowicz, G. et al. Quantum guidelines for solid-state spin defects. *Nat. Rev. Mater.* **6**, 906–925 (2021).
7. Kinos, A. et al. Roadmap for rare-earth quantum computing (2021). 2103.15743.
8. Ourari, S. et al. Indistinguishable telecom band photons from a single Er ion in the solid state. *Nature* **620**, 977–981 (2023).
9. Duan, L.-M., Lukin, M. D., Cirac, J. I. & Zoller, P. Long-distance quantum communication with atomic ensembles and linear optics. *Nature* **414**, 413–418 (2001).
10. Craiciu, I. et al. Nanophotonic quantum storage at telecommunication wavelength. *Phys. Rev. Appl.* **12**, 024062 (2019).
11. Dutta, S. et al. An Atomic Frequency Comb Memory in Rare-Earth-Doped Thin-Film Lithium Niobate. *ACS Photonics* **10**, 1104–1109 (2023).
12. Lago-Rivera, D., Grandi, S., Rakonjac, J. V., Seri, A. & de Riedmatten, H. Telecom-heralded entanglement between multimode solid-state quantum memories. *Nature* **594**, 37–40 (2021).
13. Bartholomew, J. G. et al. On-chip coherent microwave-to-optical transduction mediated by ytterbium in YVO4. *Nat. Commun* **11**, 3266 (2020).
14. O'Brien, C., Lauk, N., Blum, S., Morigi, G. & Fleischhauer, M. Interfacing superconducting qubits and telecom photons via a rare-earth-doped crystal. *Phys. Rev. Lett.* **113**, 063603 (2014).
15. Lauritzen, B. et al. Telecommunication-wavelength solid-state memory at the single photon level. *Phys. Rev. Lett.* **104**, 080502 (2010).
16. Dajczgewand, J., Gouët, J.-L. L., Louchet-Chauvet, A. & Chanelière, T. Large efficiency at telecom wavelength for optical quantum memories. *Opt. Lett.* **39**, 2711–2714 (2014).
17. Razavi, M., Piani, M. & Lütkenhaus, N. Quantum repeaters with imperfect memories: Cost and scalability. *Phys. Rev. A* **80**, 032301 (2009).
18. Rančić, M., Hedges, M. P., Ahlefeldt, R. L. & Sellars, M. J. Coherence time of over a second in a telecom-compatible quantum memory storage material. *Nat. Phys.* **14**, 50–54 (2018).
19. Probst, S., Rotzinger, H., Ustinov, A. V. & Bushev, P. A. Microwave multimode memory with an erbium spin ensemble. *Phys. Rev. B* **92**, 014421 (2015).
20. Chirolli, L. & Burkard, G. Decoherence in solid-state qubits. *Adv. Phys.* **57**, 225–285 (2008).
21. Kanai, S. et al. Generalized scaling of spin qubit coherence in over 12,000 host materials. *PNAS* **119**, e2121808119 (2022).
22. Anderson, C. P. et al. Five-second coherence of a single spin with single-shot readout in silicon carbide. *Sci. Adv.* **8**, eabm5912 (2022).
23. Balasubramanian, G. et al. Ultralong spin coherence time in isotopically engineered diamond. *Nat. Mater* **8**, 383–387 (2009).
24. Bourassa, A. et al. Entanglement and control of single nuclear spins in isotopically engineered silicon carbide. *Nat. Mater* **19**, 1319–1325 (2020).
25. Dantec, M. L. et al. Twenty-three-millisecond electron spin coherence of erbium ions in a natural-abundance crystal. *Sci. Adv.* **7**, eabj9786 (2021).
26. Rančić, M. et al. Electron-spin spectral diffusion in an erbium doped crystal at millikelvin temperatures. *Phys. Rev. B* **106**, 144412 (2022).
27. Grant, G. D. et al. Optical and microstructural characterization of Er^{3+} doped epitaxial cerium oxide on silicon. *APL Mater* **12**, 021121 (2024).
28. Raha, M. et al. Optical quantum nondemolition measurement of a single rare earth ion qubit. *Nat. Commun* **11**, 1605 (2020).
29. Welinski, S. et al. Electron spin coherence in optically excited states of rare-earth ions for microwave to optical quantum transducers. *Phys. Rev. Lett.* **122**, 247401 (2019).
30. Xie, T. et al. Characterization of er^{3+}: YVo_4 for microwave to optical transduction. *Phys. Rev. B* **104**, 054111 (2021).
31. Ammerlaan, C. A. J. & de Maat-Gersdorf, I. Zeeman splitting factor of the Er3+ ion in a crystal field. *Appl. Magn. Reson.* **21**, 13–33 (2001).
32. Liu, G. & Jacquier, B.*Spectroscopic Properties of Rare Earths in Optical Materials* (Springer Berlin, Heidelberg, 2005).
33. Singh, M. K. et al. Epitaxial Er-doped Y2O3 on silicon for quantum coherent devices. *APL Mater* **8**, 31111 (2020).
34. Dibos, A. M. et al. Purcell enhancement of erbium ions in tio2 on silicon nanocavities. *Nano Lett.* **22**, 6530–6536 (2022).
35. Sun, Y., Thiel, C., Cone, R., Equall, R. & Hutcheson, R. Recent progress in developing new rare earth materials for hole burning and coherent transient applications. *J. Lumin.* **98**, 281–287 (2002).
36. Stevenson, P. et al. Erbium-implanted materials for quantum communication applications. *Phys. Rev. B* **105**, 224106 (2022).
37. Phenicie, C. M. et al. Narrow optical line widths in erbium implanted in tio2. *Nano Lett.* **19**, 8928–8933 (2019). PMID: 31765161.
38. Abella, I. D., Kurnit, N. A. & Hartmann, S. R. Photon echoes. *Phys. Rev.* **141**, 391–406 (1966).
39. Macfarlane, R. M., Harris, T. L., Sun, Y., Cone, R. L. & Equall, R. W. Measurement of photon echoes in er:y2sio5 at 1.5 μm with a diode laser and an amplifier. *Opt. Lett.* **22**, 871–873 (1997).
40. Böttger, T., Thiel, C. W., Sun, Y. & Cone, R. L. Optical decoherence and spectral diffusion at 1.5μm in er^{3+}: y_2sio_5 versus magnetic field, temperature, and er^{3+} concentration. *Phys. Rev. B* **73**, 075101 (2006).
41. Liu, G. K. & Cone, R. L. Laser-induced instantaneous spectral diffusion in tb^{3+} compounds as observed in photon-echo experiments. *Phys. Rev. B* **41**, 6193–6200 (1990).
42. Könz, F. et al. Temperature and concentration dependence of optical dephasing, spectral-hole lifetime, and anisotropic absorption in eu^{3+}: Y_2sio_5. *Phys. Rev. B* **68**, 085109 (2003).
43. Sun, Y., Thiel, C. W. & Cone, R. L. Optical decoherence and energy level structure of 0.1%tm^{3+}: $linbo_3$. *Phys. Rev. B* **85**, 165106 (2012).
44. Anderson, P. W., Halperin, B. I. & Varma, C. M. Anomalous low-temperature thermal properties of glasses and spin glasses. *Philos. Mag.* **25**, 1–9 (1972).

45. Huber, D. L., Broer, M. M. & Golding, B. Low-temperature optical dephasing of rare-earth ions in glass. *Phys. Rev. Lett.* **52**, 2281–2284 (1984).
46. Flinn, G. P. et al. Sample-dependent optical dephasing in bulk crystalline samples of y_2o_3: eu^{3+}. *Phys. Rev. B* **49**, 5821–5827 (1994).
47. Bartholomew, J. G., de Oliveira Lima, K., Ferrier, A. & Goldner, P. Optical line width broadening mechanisms at the 10 khz level in eu3+:y2o3 nanoparticles. *Nano Letters* **17**, 778–787 (2017).
48. Serrano, D. et al. Ultra-narrow optical linewidths in rare-earth molecular crystals. *Nature* **603**, 241–246 (2022).
49. Fukumori, R., Huang, Y., Yang, J., Zhang, H. & Zhong, T. Subkilohertz optical homogeneous linewidth and dephasing mechanisms in er^{3+}: y_2o_3 ceramics. *Phys. Rev. B* **101**, 214202 (2020).
50. Dibos, A. M., Raha, M., Phenicie, C. M. & Thompson, J. D. Atomic source of single photons in the telecom band. *Phys. Rev. Lett.* **120**, 243601 (2018).
51. Zhong, T. et al. Optically addressing single rare-earth ions in a nanophotonic cavity. *Phys. Rev. Lett.* **121**, 183603 (2018).
52. Rakhmatullin, R. M., Kurkin, I. N., Pavlov, V. V. & Semashko, V. V. Epr, optical, and dielectric spectroscopy of er-doped cerium dioxide nanoparticles. *Phys. Status Solidi B* **251**, 1545–1551 (2014).
53. Salikhov, K., Dzuba, S. & Raitsimring, A. The theory of electron spin-echo signal decay resulting from dipole-dipole interactions between paramagnetic centers in solids. *J. Magn. Reson.* **42**, 255–276 (1981).
54. Eichhorn, T. R., McLellan, C. A. & Bleszynski Jayich, A. C. Optimizing the formation of depth-confined nitrogen vacancy center spin ensembles in diamond for quantum sensing. *Phys. Rev. Mater.* **3**, 113802 (2019).
55. Tyryshkin, A. M. et al. Electron spin coherence exceeding seconds in high-purity silicon. *Nat. Mater* **11**, 143–147 (2012).
56. Candido, D. R. & Flatté, M. E. Interplay between charge and spin noise in the near-surface theory of decoherence and relaxation of c_{3v} symmetry qutrit spin-1 centers (2023).
57. Car, B., Veissier, L., Louchet-Chauvet, A., Le Gouët, J.-L. & Chanelière, T. Optical study of the anisotropic erbium spin flip-flop dynamics. *Phys. Rev. B* **100**, 165107 (2019).
58. Hastings-Simon, S. R. et al. Zeeman-level lifetimes in er^{3+}: y_2sio_5. *Phys. Rev. B* **78**, 085410 (2008).
59. Kurkin, I. & Chernov, K. Epr and spin-lattice relaxation of rare-earth activated centres in y2sio5 single crystals. *Physica B+C* **101**, 233–238 (1980).
60. Abragam, A. & Bleaney, B.*Electron paramagnetic resonance of transition ions* (Oxford, 1986).
61. Lutz, T. et al. Modification of phonon processes in nanostructured rare-earth-ion-doped crystals. *Phys. Rev. A* **94**, 013801 (2016).
62. Orbach, R. Spin-lattice relaxation in rare-earth salts. *Proc. R. Soc. Lond. A* **264**, 458–484 (1961).
63. Gupta, S., Wu, X., Zhang, H., Yang, J. & Zhong, T. Robust millisecond coherence times of erbium electron spins. *Phys. Rev. Appl.* **19**, 044029 (2023).
64. Kindem, J. M. et al. Control and single-shot readout of an ion embedded in a nanophotonic cavity. *Nature* **580**, 201–204 (2020).
65. Jiang, L. et al. Repetitive readout of a single electronic spin via quantum logic with nuclear spin ancillae. *Science* **326**, 267–272 (2009).
66. Lee, S.-Y. et al. Readout and control of a single nuclear spin with a metastable electron spin ancilla. *Nat. Nanotechnol* **8**, 487–492 (2013).
67. Nishikawa, Y., Fukushima, N., Yasuda, N., Nakayama, K. & Ikegawa, S. Electrical properties of single crystalline ceo2 high-k gate dielectrics directly grown on si (111). *Jpn. J. Appl. Phys.* **41**, 2480 (2002).
68. Oh, C.-S., Kim, C.-I. & Kwon, K.-H. Etch characteristics of CeO2 thin films as a buffer layer for the application of ferroelectric random access memory. *J. Vac. Sci. Technol. A* **19**, 1068–1071 (2001).
69. Kossoy, A., Greenberg, M., Gartsman, K. & Lubomirsky, I. Chemical reduction and wet etching of ceo2 thin films. *J. Electrochem. Soc.* **152**, C65 (2005).

Acknowledgements

The authors would like to thank Dr. Yeghishe Tsaturyan for helpful discussions. This work was primarily funded by the U.S. Department of Energy, Office of Science, Basic Energy Sciences, Materials Sciences and Engineering Division, including support for optical and spin characterization studies. The sample growth along with additional support for cryo-optical measurements was funded by Q-NEXT, a U.S. Department of Energy Office of Science National Quantum Information Science Research Centers under Award Number DE-FOA-0002253. The EPR work in the Chemical Sciences and Engineering Division was supported by the U.S. Department of Energy, Office of Science, Office of Basic Energy Sciences, Division of Chemical Sciences, Geosciences, and Biosciences, through Argonne National Laboratory under Contract No. DE-AC02-06CH11357. Additional experimental support was from Air Force Research Office (AFOSR) under award number FA9550–23-1-0667.

Author contributions

J.Z. conceived the experiments and performed the data analysis. J.Z. and G.D.G. carried out the optical measurements. I.M. carried out the growth of the sample with assistance from G.D.G. M.T.S. and A.M.D. helped carry out the fridge and optical echo measurements. J.C.M. helped analyze spin coherence data. J.K.B., J.N., and O.G.P. helped carry out the pulsed EPR measurements. All authors contributed to the manuscript.

Competing interests

The authors declare no competing interests.

Additional information

Supplementary information The online version contains supplementary material available at https://doi.org/10.1038/s41534-024-00903-z.

Correspondence and requests for materials should be addressed to Jiefei Zhang or Supratik Guha.